Contents lists available at ScienceDirect

Scripta Materialia

journal homepage: www.journals.elsevier.com/scripta-materialia

Fatigue and fracture of shape memory alloys in the nanoscale: An *in-situ* TEM study

R. Sidharth [a], J.C. Stinville [b], H. Sehitoglu [a,*]

[a] Department of Mechanical Science and Engineering, University of Illinois at Urbana-Champaign, 1206W. Green St., Urbana, IL 61801, USA
[b] Department of Materials Science and Engineering, University of Illinois at Urbana-Champaign, 1304W. Green St., Urbana, IL 61801, USA

ARTICLE INFO

Keywords:
In-situ TEM
Superelasticity
Functional fatigue
Structural fatigue
Nanomechanical testing
Shape memory alloys

ABSTRACT

This study is aimed at demonstrating the fatigue and fracture mechanisms in nanoscale NiTi shape memory alloy thin films. During functional fatigue, permanent strains are attributed to residual martensite pinned by Ni_4Ti_3 precipitates and interfacial dislocations parallel to type II internal twins of the martensite. These residual martensite-austenite interfaces acted as heterogeneous nucleation sites for stress-induced martensite in subsequent cycles thereby explaining the reduction in transformation stress. Finally, structural failure was observed to occur along the dislocation-rich austenite-martensite interface, making it the weakest link in the microstructure thus establishing a direct link between mechanisms of functional fatigue that result in the accumulation of permenant strain and mechanisms of structural fatigue that result in fracture. This work provides a comprehensive understanding of deformation mechanisms in nanoscale shape memory alloys and points to fundamental mechanisms that are applicable to macro scales.

Shape memory alloys (SMAs) have been around for nearly 75 years [1]. Since its discovery in 1963, NiTi has become one of today's most successful shape memory alloys. Under the right temperature condition, an austenitic to martensitic phase transformation, resulting in large strain accommodation, can be achieved by applying an external load. Reversal of this phase transformation by unloading (superelastic effect) or unloading followed by heating (shape memory effect) recovers almost all the strain, with some irrecoverability that accumulates upon cycling. Due to their unique functional properties, SMAs are used in engineering applications like biomedical stents, solid-state actuators, active/passive damping, and elastocaloric cooling, to name a few [2–7]. Barring the extensive applications of SMAs in macro-scale applications, there is immense interest in exploiting SMAs in the small length scales such as in micro-stents, micro-valves, micro-pumps, actuators in micro/nano-electro-mechanical systems (MEMS/NEMS), and biomimetic systems [8–19]. It is, therefore, imperative to understand the nanoscale mechanisms that enable the functionality of shape memory alloys. Moreover, nanoscale shape memory alloys' fatigue and fracture behavior are unknown.

Superelasticity in the micro to the nanoscale has been primarily studied by pillar compression tests with pillar diameters ranging from 2 μm to 140 nm [18,20–28]. One study demonstrated that superelasticity vanishes below 200 nm [22], whereas another study [24] reports superelasticity in a 140 nm pillar. However, studies reporting nanomechanical tensile behavior of shape memory dogbone thin films are scarce. Few studies report tensile straining of NiTi thin films [29,30] but not the fatigue behavior. The dynamic aspects of stress-induced martensite nucleation, growth, shrinkage, and accumulation of unrecovered strain have not been observed in real-time before. Due to dimensional constraints, electron transparency is limited for micropillars. On the other hand, in-situ TEM tensile testing would circumvent this issue as the sample thickness can reach electron transparent levels. Here, we demonstrate superelasticity in NiTi thin films with a thickness of the order of 100 nm and the width/length of the order of couple micrometers therefore representing the plane stress condition. Nanomechanical tensile fatigue of electron transparent NiTi thin films was carried out for multiple cycles. The stress-induced reversible martensitic transformation was observed with unprecedented clarity to reveal the underlying mechanisms behind unrecovered strains and fracture behavior.

To realize these findings, site-specific sample fabrication was employed using the focused ion beam milling (FIB) technique coupled with a Bruker™ push-to-pull device (Fig. 1a) and Hysitron PI95 Picoindenter. Such a push-to-pull device has been employed before to

* Corresponding author.
E-mail address: huseyin@illinois.edu (H. Sehitoglu).

https://doi.org/10.1016/j.scriptamat.2023.115577
Received 15 March 2023; Received in revised form 9 May 2023; Accepted 23 May 2023

study the mechanical behavior of nanofibers, polymers, pure metals, and oxides [31–37]. Single crystals of $Ni_{50.8}Ti$ (at%) were grown using the Bridgeman technique, solutionized at 920 °C for 2 h in argon, and water quenched. Then, miniature blocks of 4 × 4 × 8 mm^3 dimension were EDM cut and aged at 550 °C for 1.5 h to introduce homogenous lenticular Ni_4Ti_3 precipitates[38]. The transformation temperatures obtained via differential scanning calorimetry (DSC) were as follows: Austenite start (A_s) = −18 °C, Austenite finish (A_f) = 1 °C, Martensite start (M_s) = −55 °C and Martensite finish (M_f) = −70 °C. This heat treatment results in a single-step stress-induced B2 austenite to B19' martensite phase transformation at room temperature.

The crystallographic orientation of the EDM-cut blocks was identified as [101], $[1\bar{3}\bar{1}]$ and $[\bar{2}12]$ using electron backscattered diffraction (EBSD). FIB lift-out samples were extracted from the [101] plane with $[11\bar{1}]$ foil normal corresponding to the $[\bar{1}21]$ loading direction. These FIB samples were first pre-thinned to 800 nm on the conventional TEM copper grid at 30 kV and 0.43 nA probe current. Then the sample was transferred onto the push-to-pull device using the Autoprobe™ micromanipulator needle and attached by depositing platinum (see supplementary materials). The lamella was then thinned down to an electron transparent level of ≈100 nm at 30 kV accelerating voltage and a current of 0.23 nA and then at a current of 80 pA. Final thinning was done at 5 kV and 48 pA probe current to obtain high-quality TEM samples suitable for simultaneous imaging and nanomechanical tensile testing (Fig. 1b).

Hysitron PI95 Picoindenter was used for the nanomechanical test. An in-situ tensile test was performed in a JOEL 2010 LaB_6 TEM operating at 200 kV accelerating voltage. Once the sample was tilted to achieve the appropriate diffraction and contrast condition, the diamond indenter was fine aligned with the PTP. The samples were loaded under displacement control at the rate of 3–5 nm/s resulting in a strain rate of 5×10^{-4} to 1.3×10^{-3} s^{-1}. The engineering strain was calculated by manually measuring the displacement of microstructural markers in the sample, and engineering stress was calculated from the measured load. PTP stiffness, measured after sample failure, ranged from 400 to 500 N/m, close to the manufacturer's specification of 450 N/m. The load carried by the PTP was subtracted from the total load to obtain the load carried by the micro-tensile sample. Videos were captured during *insitu* loading using the Gatan SC1000 CCD camera at 1fps, 4000 × 2600 pixel resolution. Transformation stress was obtained by visually extracting the timestep at the onset of transformation and aligning it with the load vs time plots.

Cycle 2 stress-strain loop is shown in Fig. 2. As shown in the inset of TEM snapshot A in Fig. 2, the zone axis belongs to ⟨111⟩. Before loading, the sample's initial microstructure consisted of residual martensite from cycle 1 (not shown here) and two precipitate variants with longitudinal axis parallel to $[1\bar{1}0]_{B2}$and $[0\bar{1}\bar{1}]_{B2}$, the former being the dominant one with a volume fraction of ≈20%. A maximum displacement of 150 nm, corresponding to a maximum strain of 5.3%, was applied. At a stress value of about 392 MPa corresponding to the axial strain of 0.85%, martensite nucleates along the interface of precipitate variant 2, as shown by the red arrow in TEM snapshot B in Fig. 2 (see supplementary video 1). As the applied displacement is increased, new martensite variants nucleate and grow. However, a stress plateau or a slope change was not observed. This suggests that a nanoscopic nuclei of martensite appear in the so-called elastic regime, well before the stress-strain curve deviates from linearity. This was also observed in bulk samples when a considerable temperature change, indicative of latent heat release during the austenite to martensite transformation, was measured in the elastic regime of the stress-strain curve [39]. Once the stress reaches a value of about 682 MPa, the internally twinned residual martensite domains grow (TEM snapshot C in Fig. 2). This results in intrinsic softening, as evidenced by a gradual stress drop due to unpinning of the residual martensite-austenite interface. However, due to intermittent pinning of the interface at precipitate interfaces, tiny stress jumps can be seen (inset of stress displacement curve in Fig. 2). Pinning and unpinning of these interfaces explains the serrated yield plateau commonly observed during bulk deformation of shape memory alloys. Additionally, the movement of the residual martensite-austenite interface is facilitated by the growth of the internal twins, i.e., detwinning which also gives rise to intrinsic softening. The width of the residual martensite domains is visibly larger as loading reaches a maximum displacement of 150 nm and 668 MPa stress corresponding to a stress drop magnitude of 14 MPa. During the unloading stage, martensite needles begin to shrink. A few 'pop-ins' are observed in the stress-displacement curve (point E in Fig. 2); this corresponds to unpinning the residual martensite-austenite interface, which facilitates sudden retraction of the interface leading to a jump in displacement magnitude. The unloaded microstructure (TEM snapshot F in Fig. 2), shows that the residual martensite domains have grown. They seem to be pinned at the tips of precipitate variant 1 and the interface of precipitate variant 2 (red arrows in the TEM snapshot F in Fig. 2). The SAD pattern reveals one of the orientation relationships between B2 and B19' as $[11\bar{1}]_{B2} \| [1\bar{1}0]_{B19'}$ and martensite twinning was identified as type II with $[1\bar{1}0]_{B19'} \| [\bar{1}01]_{B19'}$. This means every $(11\bar{1})_{B2}$plane transforms into a $(1\bar{1}0)_{B19'}$ plane during loading and vice versa during unloading. The precipitate shares $\{111\}_{B2}$as the habit plane with the austenite. So based on the precipitate stress field and the orientation relationship between austenite and martensite, the precipitate-B2 interface is the most conducive location for martensite nucleation. Additionally, introducing precipitates starve the surrounding matrix of Ni leading to an increase in M_s [40,41] and also generates an internal stress field that interacts with the external stress to preferentially nucleate specific martensitic habit plane variants [40,42–44]. It was also observed that martensite moves along the said interface and

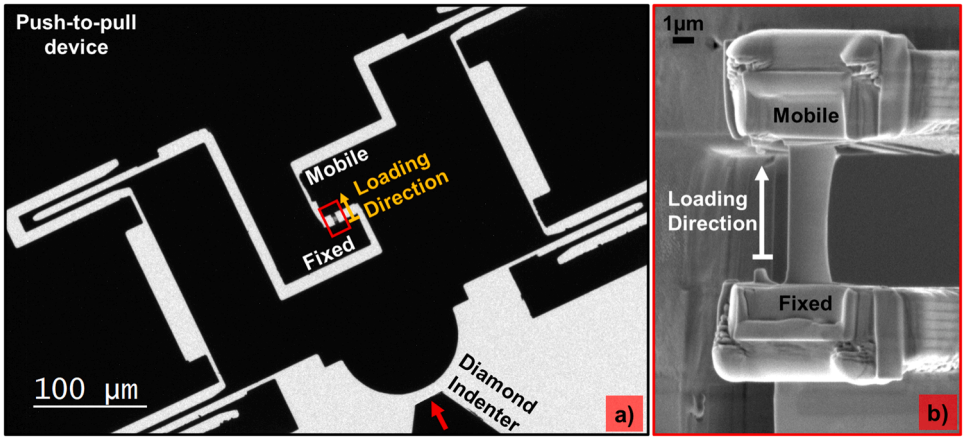

Fig. 1. (a) Push-to-pull device and conical, flat punch diamond indenter. (b) Higher magnification of electron transparent tensile sample.

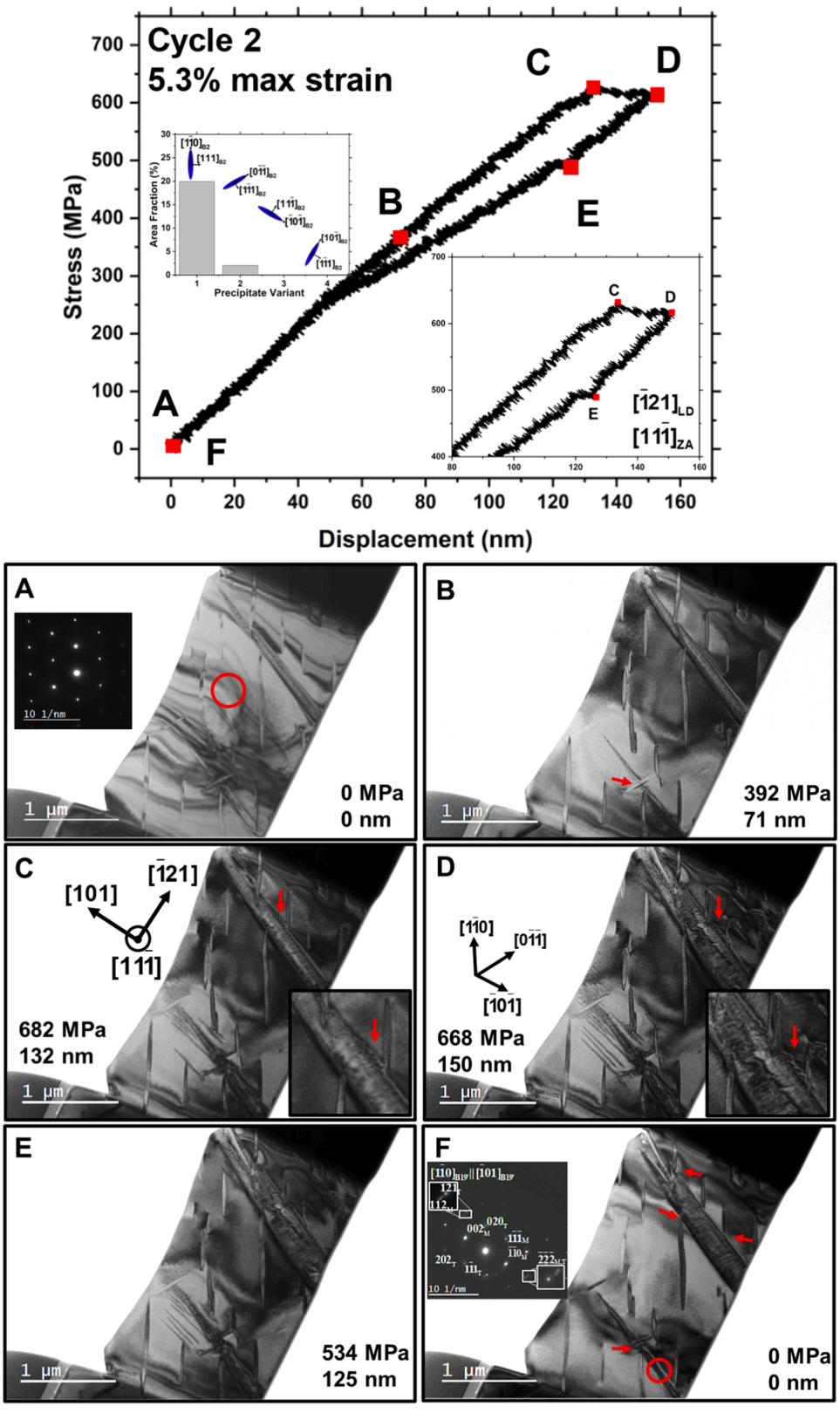

Fig. 2. The stress displacement curve for cycle 2 with the precipitate volume fraction as inset. Superelastic behavior is evident. The stress drop and the stress pop-in are visible during loading and unloading, respectively. They correspond to unpinning of the austenite-residual martensite interface to facilitate growth/shrinkage during loading/unloading. A to F are the TEM bright field images corresponding to points (A, B, C, D, E, and F) annotated in the stress-displacement curve. Martensite nucleation and growth are visible. Martensite appears pinned by the tips/interface of the precipitate after unloading. The residual martensite has $[11\bar{1}]_{B2}\|[1\bar{1}0]_{B19'}$ orientation relationship and the martensite twinning was identified as type II with $[1\bar{1}0]_{B19'}\|[\bar{1}01]_{B19'}$ as evidenced from the SADP (inset of F). See supplementary video 1.

gets pinned at the interface/tips during unloading. The coherency stress field is larger near the tips as pointed out in experimental and computational studies [45] and itcould play a role. This suggests that the precipitates aid in the forward (austenite to martensite) transformation. However, they impede the reverse transformation.

Next, these samples were loaded to the same maximum displacement for over 25 cycles. As shown in Fig. 3, the transformation stress gradually decreases, and internally twinned residual martensite accumulates in the microstructure. Consequently, the stiffness reduces from 790 N/m in cycle 2 to 540 N/m in cycle 25. The higher magnification bright field TEM image, taken after cycle 14 (Fig. 3), clearly shows parallel dislocations at the residual martensite-austenite interface. In our previous

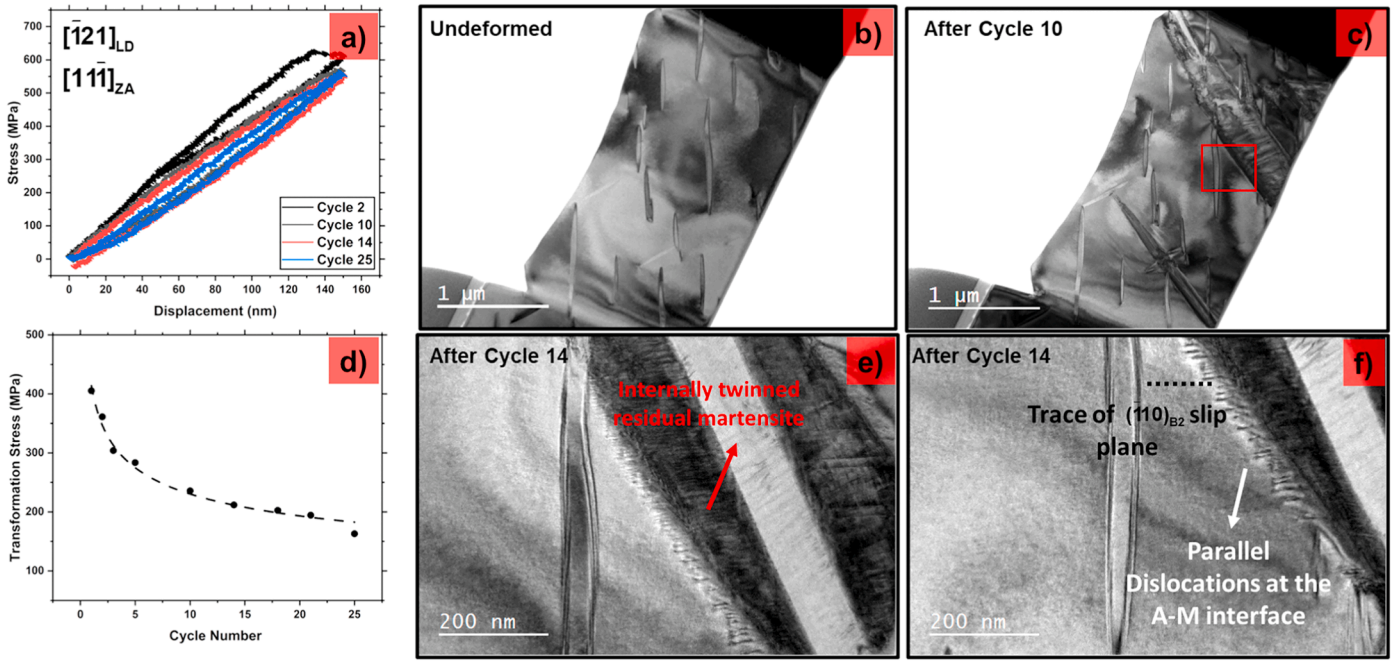

Fig. 3. Fatigue loading of the *in-situ* TEM sample for over 25 cycles. (a) Stress displacement curves. (b) Microstructure of the undeformed sample. (c) Upon fatiguing for ten cycles, residual martensite accumulates in the microstructure. (d) The reduction in transformation stress. (e) and (f) The residual martensite domains are pinned by parallel dislocations at the austenite-martensite interface. The dislocations originate from the internal twins of the martensite.

experimental and modeling work [39,46], we showed that these dislocations could be traced back to the internal twins of the martensite. During reverse movement of the austenite-martensite boundary, the type I or type II internal twins of the martensite transform to parallel dislocations on the <111>{011}$_{B2}$ or <100>{011}$_{B2}$ slip system, respectively, based on lattice correspondence. At this point, it should be noted that the most energetically favorable slip system is the <100>{011} [47]. The type of internal twins of the martensite depends on the martensite correspondent variant pair (CVP) activated, which in turn depends on the local resolved shear stress due to the applied stress and the local stress field of the precipitate variant present [42]. As the CRSS to move a dislocation in NiTi is much higher than the CRSS for transformation [47], once the internal twin transforms to parallel dislocations during unloading, these dislocations become sessile and pin the interface. This stabilizes martensite even after unloading, thereby giving rise to residual strain. As seen clearly in Fig. 3, these dislocations are parallel to the internal twins of the residual martensite. The internal twinning of the martensite is identified to belong to type II from the diffraction pattern shown in the inset of Fig. 1F. Directly identifying the slip system of these dislocations in the current experiments is not possible due to the absence of double tilt capability in the picoindenter, however the dislocation trace is parallel to the trace of $(\bar{1}10)_{B2}$slip plane. To provide clear insight into the microstructural mechanisms behind the reduction in transformation stress and the accumulation of residual martensite, in-situ TEM experiments performed at higher magnification are discussed next.

High-magnification snapshots taken during cycles 11 and 12 are presented in Fig. 4 (also see supplementary videos 2 and 3). During loading, at 248 MPa, martensite needles nucleate from the interface of precipitate variant 2 (Fig. 4a), tips of residual martensite (Fig. 4a), and the residual martensite-austenite interface (Fig. 4b). The parallel dislocations at the austenite-martensite interface aid in the nucleation of fresh martensite needles. This leads to the reduction in transformation stress in the subsequent fatigue cycle. The nucleation barrier for stress-induced martensite is significantly reduced with additional nucleation sites, such as the residual martensite interface, which offers an internal stress field to assist transformation. As the applied displacement is increased further, at 600 MPa, fresh martensite needles nucleate from the tips of precipitate variant 1 (Fig. 4a). During unloading, martensite needles recede to their point of nucleation along the same path. Martensite needles that nucleated from the residual martensite tips/interface do not recover completely and get pinned at the tips/interface, contributing to the accumulation of residual strain (compare snapshots taken at 0 nm and unloaded state in Fig. 4). Gradually, by this process, the residual martensite domains grow. One can also see that martensite gets pinned at the interface of the precipitate (see unloaded state in Fig. 4a). Finally, after 25 cycles of fatigue deformation, the thin film sample was pulled to failure—a crack initiated from a notch that was created during the sample fabrication. As the sample was pulled to failure, the stress-strain behavior exhibited a hardening-type response until, as shown in Fig. 5, crack propagated to failure along the austenite-martensite interface at 790 MPa. This makes sense as the dislocation-rich interface is the weakest link in the microstructure. Even though the crack nucleated from a notch, the crack preferred to propagate along the austenite-martensite interface. Therefore, these in-situ TEM observations provide a direct physically-rooted link between the mechanisms of functional fatigue that accumulate permanent strain and mechanisms of structural fatigue that result in fracture. Similar observations of cracking along the A-M interface were made on fatigued bulk FeMnAlNi, FeMnAlNiTi and CuZnAl SMAs [48–50].

Even though these observations were made during the nano-mechanical fatigue testing of NiTi SMA, the underlying mechanisms for fatigue degradation could be applicable in the bulk state as well. Introducing Ni_4Ti_3 precipitates in NiTi SMA is commonly thought as beneficial for superelasticity and fatigue resistance, however it was shown in this study that precipitates aid forward transformation but seem to restrict reverse transformation by pinning martensite. This mechanism can be translated to micro and bulk samples. Recent studies on NiTi micropillars have revealed dislocation activity around precipitates [44] and dislocations even shear into the precipitates in bulk samples [39]. Additionally, it was also shown that the transformation induced dislocations stem from the internal twins of the martensite. So, one can conceive that, during unloading, these dislocations get pinned at the precipitate-B2 interface due to the coherency stress field which in

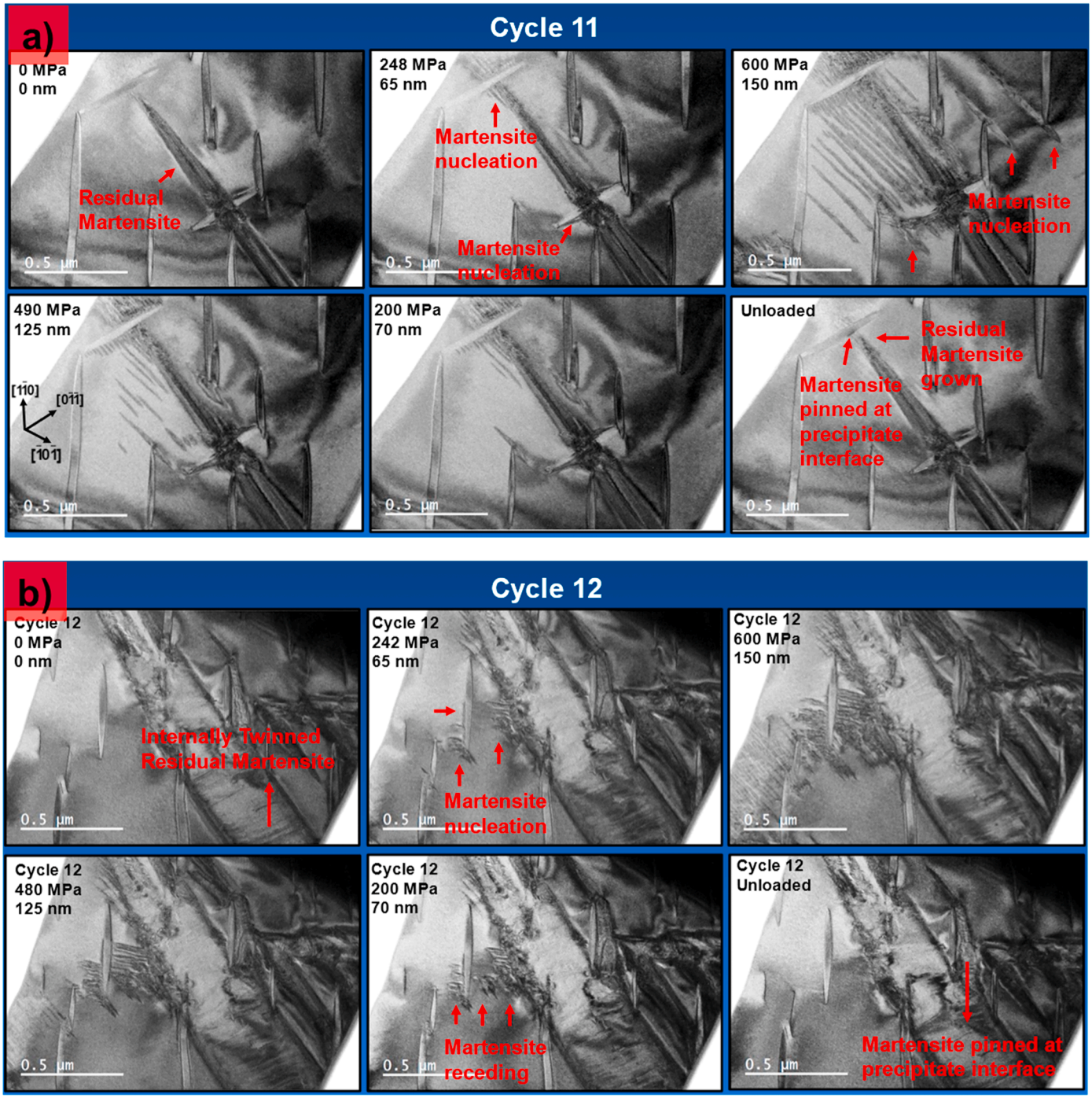

Fig. 4. Higher magnification TEM snapshots were taken during the loading/unloading of (a) cycle 11 and (b) 12. Martensite nucleation from the residual martensite-austenite interface from prior cycles can be evidenced. During unloading, these martensite needles do not recover completely, get pinned, and result in the net growth of the residual martensite domains. Furthermore, residual martensite pinned at the interface of precipitates can be seen as well. See supplementary videos 2 and 3.

turn pins the austenite-martensite interface in the nano-samples. However, in the bulk samples, the austenite-martensite interface can be relatively glissile and only the transformation induced dislocations get pinned leading to the formation of elongated dislocation segments during martensite shrinkage as evidenced in our earlier work [39]. Nevertheless, residual martensite has also been observed in other studies reporting cyclic deformation of micro and bulk NiTi [51–54]. Therefore, the stabilization and accumulation of residual martensite domains in bulk could be facilitated via the same mechanisms reported in this study.

In conclusion, this study has demonstrated that excellent superelasticity can be achieved in NiTi shape memory alloy nanoscale thin films. A clear understanding of martensite nucleation, growth, and shrinkage was achieved by directly observing the stress-induced martensitic transformation in the nanoscale volumes. The microstructural mechanism behind the accumulation of residual martensite and the source of martensite pinning was uncovered in real-time. This study confirmed some previously proposed functional degradation mechanisms, such as parallel dislocations emanating from type II internal twins of the martensite, and uncovered new mechanisms, such as martensite pinning by precipitate tips/interfaces. Finally, a direct link between functional fatigue and structural failure was established by demonstrating fracture along the dislocation rich austenite-martensite

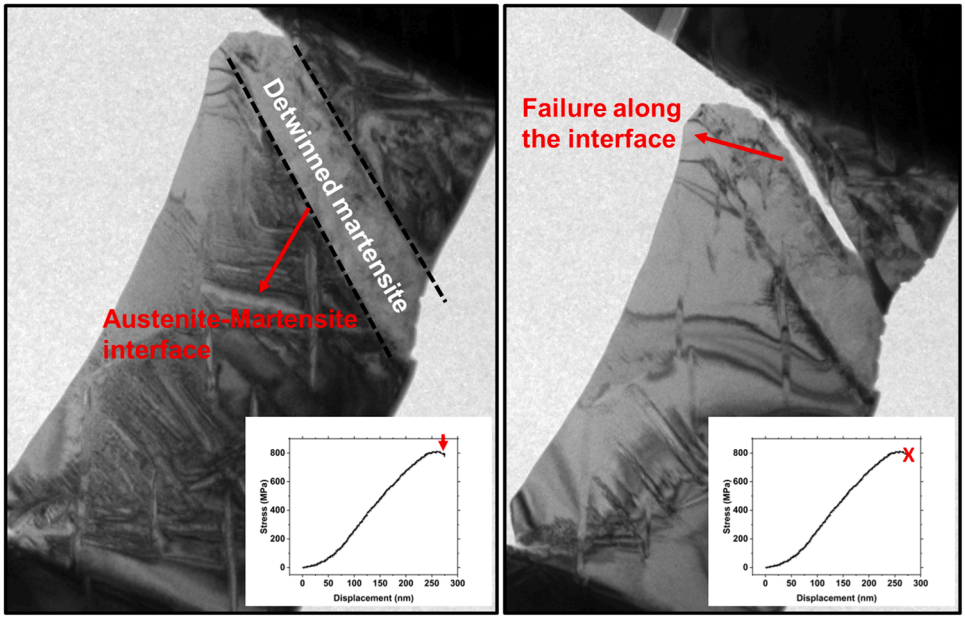

Fig. 5. Fracture along the dislocation-rich austenite-martensite interface. A direct link between functional fatigue mechanism and structural failure is demonstrated. See supplementary video 4.

interface.

Declaration of Competing Interest

The authors declare that they have no known competing financial interests or personal relationships that could have appeared to influence the work reported in this paper.

Acknowledgments

This work is supported by the National Science Foundation Grant DMR- 2104971, Metallic Materials and Nanomaterials Program, which is gratefully acknowledged. SEM, FIB, TEM and EBSD were carried out in part in the Frederick Seitz Materials Research Laboratory Central Research Facilities, University of Illinois Urbana-Champaign.

Supplementary materials

Supplementary material associated with this article can be found, in the online version, at doi:10.1016/j.scriptamat.2023.115577.

References

[1] L.C. Chang, T. Read, Plastic deformation and diffusionless phase changes in metals—The gold-cadmium beta phase, JOM 3 (1951) 47–52.
[2] D.C. Lagoudas, Shape Memory alloys: Modeling and Engineering Applications, Springer, 2008.
[3] D.J. Hartl, D.C. Lagoudas, Aerospace applications of shape memory alloys, Proc. Inst. Mech. Eng. Part G J. Aerosp. Eng. 221 (4) (2007) 535–552.
[4] D. Safranski, K. Dupont, K. Gall, Pseudoelastic NiTiNOL in orthopaedic applications, Shape Memory and Superelasticity 6 (3) (2020) 332–341.
[5] T.W. Duerig, The use of superelasticity in modern medicine, MRS Bull. 27 (2) (2002) 101–104.
[6] E.A. Williams, G. Shaw, M. Elahinia, Control of an automotive shape memory alloy mirror actuator, Mechatronics 20 (5) (2010) 527–534.
[7] J.V. Humbeeck, S. Kustov, Active and passive damping of noise and vibrations through shape memory alloys: applications and mechanisms, Smart Mater. Struct. 14 (5) (2005) S171–S185.
[8] K. Bhattacharya, R.D. James, The material is the machine, Science 307 (5706) (2005) 53–54.
[9] Y. Fu, H. Du, W. Huang, S. Zhang, M. Hu, TiNi-based thin films in MEMS applications: a review, Sens. Actuators A 112 (2–3) (2004) 395–408.
[10] R.H. Wolf, A.H. Heuer, TiNi (shape memory) films silicon for MEMS applications, J. Microelectromech. Syst. 4 (4) (1995) 206–212.
[11] M. Kohl, Shape Memory Microactuators, Springer Science & Business Media2004.
[12] S.A. Wilson, R.P. Jourdain, Q. Zhang, R.A. Dorey, C.R. Bowen, M. Willander, Q. U. Wahab, S.M. Al-hilli, O. Nur, E. Quandt, New materials for micro-scale sensors and actuators: an engineering review, Mater. Sci. Eng. R Rep. 56 (1–6) (2007) 1–129.
[13] C.R. Knick, D.J. Sharar, A.A. Wilson, G.L. Smith, C.J. Morris, H.A. Bruck, High frequency, low power, electrically actuated shape memory alloy MEMS bimorph thermal actuators, J. Micromech. Microeng. 29 (7) (2019), 075005.
[14] Y.Q. Fu, J. Luo, A. Flewitt, S.E. Ong, S. Zhang, H. Du, W. Milne, Microactuators of free-standing TiNiCu films, Smart Mater. Struct. 16 (6) (2007) 2651.
[15] D.J. Laser, J.G. Santiago, A review of micropumps, J. Micromech. Microeng. 14 (6) (2004) R35.
[16] E. Makino, T. Mitsuya, T. Shibata, Fabrication of TiNi shape memory micropump, Sens. Actuators A 88 (3) (2001) 256–262.
[17] P. Krulevitch, A.P. Lee, P.B. Ramsey, J.C. Trevino, J. Hamilton, M.A. Northrup, Thin film shape memory alloy microactuators, J. Microelectromech. Syst. 5 (4) (1996) 270–282.
[18] J.S. Juan, M.L. Nó, C.A. Schuh, Nanoscale shape-memory alloys for ultrahigh mechanical damping, Nat. Nanotechnol. 4 (7) (2009) 415–419.
[19] J. San Juan, M.L. Nó, C.A. Schuh, Superelasticity and shape memory in micro-and nanometer-scale pillars, Adv. Mater. 20 (2) (2008) 272–278.
[20] J. San Juan, M. Nó, C. Schuh, Superelastic cycling of Cu–Al–Ni shape memory alloy micropillars, Acta Mater. 60 (10) (2012) 4093–4106.
[21] B.G. Clark, D.S. Gianola, O. Kraft, C.P. Frick, Size independent shape memory behavior of nickel–titanium, Adv. Eng. Mater. 12 (8) (2010) 808–815.
[22] C. Frick, S. Orso, E. Arzt, Loss of pseudoelasticity in nickel–titanium sub-micron compression pillars, Acta Mater. 55 (11) (2007) 3845–3855.
[23] C.P. Frick, B.G. Clark, S. Orso, P. Sonnweber-Ribic, E. Arzt, Orientation-independent pseudoelasticity in small-scale NiTi compression pillars, Scr. Mater. 59 (1) (2008) 7–10.
[24] J. Ye, R.K. Mishra, A.R. Pelton, A.M. Minor, Direct observation of the NiTi martensitic phase transformation in nanoscale volumes, Acta Mater. 58 (2) (2010) 490–498.
[25] D. Norfleet, P. Sarosi, S. Manchiraju, M.X. Wagner, M. Uchic, P. Anderson, M. Mills, Transformation-induced plasticity during pseudoelastic deformation in Ni–Ti microcrystals, Acta Mater. 57 (12) (2009) 3549–3561.
[26] H.M. Paranjape, M.L. Bowers, M.J. Mills, P.M. Anderson, Mechanisms for phase transformation induced slip in shape memory alloy micro-crystals, Acta Mater. 132 (2017) 444–454.
[27] M. Bowers, X. Chen, M. De Graef, P.M. Anderson, M. Mills, Characterization and modeling of defects generated in pseudoelastically deformed NiTi microcrystals, Scr. Mater. 78 (2014) 69–72.
[28] R. Manjeri, S. Qiu, N. Mara, A. Misra, R. Vaidyanathan, Superelastic response of [111]and [101]oriented NiTi micropillars, J. Appl. Phys. 108 (2) (2010), 023501.
[29] W. Tirry, D. Schryvers, *In situ* transmission electron microscopy of stress-induced martensite with focus on martensite twinning, Mater. Sci. Eng. A 481 (2008) 420–425.
[30] S. Manchuraju, A. Kroeger, C. Somsen, A. Dlouhy, G. Eggeler, P. Sarosi, P. Anderson, M. Mills, Pseudoelastic deformation and size effects during *in situ* transmission electron microscopy tensile testing of NiTi, Acta Mater. 60 (6–7) (2012) 2770–2777.

[31] C. Chisholm, H. Bei, M. Lowry, J. Oh, S.S. Asif, O. Warren, Z. Shan, E.P. George, A. M. Minor, Dislocation starvation and exhaustion hardening in Mo alloy nanofibers, Acta Mater. 60 (5) (2012) 2258–2264.
[32] H. Guo, K. Chen, Y. Oh, K. Wang, C. Dejoie, S. Syed Asif, O. Warren, Z. Shan, J. Wu, A. Minor, Mechanics and dynamics of the strain-induced M1–M2 structural phase transition in individual VO2 nanowires, Nano Lett. 11 (8) (2011) 3207–3213.
[33] X. Li, J. Turner, K. Bustillo, A.M. Minor, *In situ* transmission electron microscopy investigation of electroplasticity in single crystal nickel, Acta Mater. 223 (2022), 117461.
[34] N.R. Velez, F.I. Allen, M.A. Jones, J. Donohue, W. Li, K. Pister, S. Govindjee, G. F. Meyers, A.M. Minor, Nanomechanical testing of freestanding polymer films: *in situ* tensile testing and T g measurement, J. Mater. Res. 36 (2021) 2456–2464.
[35] J. Stinville, E.R. Yao, P.G. Callahan, J. Shin, F. Wang, M.P. Echlin, T.M. Pollock, D. S. Gianola, Dislocation dynamics in a nickel-based superalloy via in-situ transmission scanning electron microscopy, Acta Mater. 168 (2019) 152–166.
[36] V. Samaeeaghmiyoni, H. Idrissi, J. Groten, R. Schwaiger, D. Schryvers, Quantitative *in-situ* TEM nanotensile testing of single crystal Ni facilitated by a new sample preparation approach, Micron 94 (2017) 66–73.
[37] V. Samaee, R. Gatti, B. Devincre, T. Pardoen, D. Schryvers, H. Idrissi, Dislocation driven nanosample plasticity: new insights from quantitative in-situ TEM tensile testing, in: Scientific Reports, 8, 2018, p. 12012.
[38] R.F. Hamilton, H. Sehitoglu, Y. Chumlyakov, H. Maier, Stress dependence of the hysteresis in single crystal NiTi alloys, Acta Mater. 52 (11) (2004) 3383–3402.
[39] R. Sidharth, A. Mohammed, H. Sehitoglu, Functional Fatigue of NiTi shape memory alloy: effect of loading frequency and source of residual strains, Shape Mem. Superelasticity 8 (2022) 1–19.
[40] Z. Li, F. Xiao, H. Chen, R. Hou, X. Cai, X. Jin, Atomic scale modeling of the coherent strain field surrounding Ni4Ti3 precipitate and its effects on thermally-induced martensitic transformation in a NiTi alloy, Acta Mater. 211 (2021), 116883.
[41] D. Schryvers, W. Tirry, Z. Yang, Measuring strain fields and concentration gradients around Ni4Ti3 precipitates, Mater. Sci. Eng. A 438 (2006) 485–488.
[42] K. Gall, H. Sehitoglu, Y.I. Chumlyakov, I.V. Kireeva, H.J. Maier, The influence of aging on critical transformation stress levels and martensite start temperatures in NiTi:part I—Aged microstructure and micro-mechanical modeling,, J. Eng. Mater. Technol. 121 (1) (1999) 19–27.
[43] K Gall, H Sehitoglu, Y.I Chumlyakov, I.V. Kireeva, H.J Maier, The influence of aging on critical transformation stress levels and martensite start temperatures in NiTi: part II—discussion of experimental results, J. Eng. Mater. Technol. (1999) 28–37.
[44] F. Xiao, K. Chu, Z. Li, R. Hou, Y. Gao, Q. Sun, X. Jin, Improved functional fatigue resistance of single crystalline NiTi micropillars with uniformly oriented Ti3Ni4 precipitates, Int. J. Plast. 160 (2023), 103480.
[45] W. Tirry, D. Schryvers, Quantitative determination of strain fields around Ni4Ti3 precipitates in NiTi, Acta Mater. 53 (4) (2005) 1041–1049.
[46] A.S.K. Mohammed, H. Sehitoglu, Martensitic twin boundary migration as a source of irreversible slip in shape memory alloys, Acta Mater. 186 (2020) 50–67.
[47] T. Ezaz, J. Wang, H. Sehitoglu, H. Maier, Plastic deformation of NiTi shape memory alloys, Acta Mater. 61 (1) (2013) 67–78.
[48] R. Sidharth, Y. Wu, F. Brenne, W. Abuzaid, H. Sehitoglu, Relationship between functional fatigue and structural fatigue of iron-based shape memory alloy FeMnNiAl, Shape Memory and Superelasticity 6 (2020) 256–272.
[49] Y. Wu, J. Yaacoub, F. Brenne, W. Abuzaid, D. Canadinc, H. Sehitoglu, Deshielding effects on fatigue crack growth in shape memory alloys-a study on cuznal single-crystalline materials, Acta Mater. 176 (2019) 155–166.
[50] R. Sidharth, W. Abuzaid, M. Vollmer, T. Niendorf, H. Sehitoglu, Fatigue crack initiation in the iron-based shape memory alloy FeMnAlNiTi, Shape Mem. Superelasticity 6 (3) (2020) 323–331.
[51] P. Hua, K. Chu, F. Ren, Q. Sun, Cyclic phase transformation behavior of nanocrystalline NiTi at microscale, Acta Mater. 185 (2020) 507–517.
[52] P. Hua, H. Lin, Q. Sun, Ultrahigh cycle fatigue deformation of polycrystalline NiTi micropillars, Scr. Mater. 203 (2021), 114108.
[53] M.F. Wagner, N. Nayan, U. Ramamurty, Healing of fatigue damage in NiTi shape memory alloys, J. Phys. D Appl. Phys. 41 (18) (2008), 185408.
[54] K. Gall, H. Maier, Cyclic deformation mechanisms in precipitated NiTi shape memory alloys, Acta Mater. 50 (18) (2002) 4643–4657.